Spontaneous Frenkel pair formation in zirconium carbide

Thomas A. Mellan,[1,*] Andrew I. Duff,[2] and Michael W. Finnis[3]

[1]*Thomas Young Centre for Theory and Simulation of Materials, Department of Materials, Imperial College London, Exhibition Road, London SW7 2AZ, United Kingdom*

[2]*STFC Hartree Centre, Scitech Daresbury, Warrington WA4 4AD, United Kingdom*

[3]*Thomas Young Centre for Theory and Simulation of Materials, Department of Physics and Department of Materials, Imperial College London, Exhibition Road, London SW7 2AZ, United Kingdom*

(Received 18 September 2018; published 30 November 2018)

With density functional theory we have performed molecular dynamics simulations of ZrC, which displayed spontaneous carbon Frenkel pair formation at a temperature of 3200 K, some 500° below the melting point. To understand this behavior, rarely seen in equilibrium simulations, we quenched and examined a set of lattices containing a Frenkel pair. Five metastable structures were found, and their formation energies and electronic properties were studied. Their thermal generation was found to be facilitated by a reduction of between 0.7 and 1.5 eV in formation energy due to thermal expansion of the lattice. With input from a quasiharmonic description of the defect-free energy of formation, an ideal solution model was used to estimate lower bounds on their concentration as a function of temperature and stoichiometry. At 3000 K (0.81 of the melting temperature) their concentration was estimated to be 1.2% per mole in a stoichiometric crystal, and 0.3% per mole in a crystal with 10% per mole of constitutional vacancies. Their contribution to heat capacity, thermal expansion, and bulk modulus was estimated.

DOI: 10.1103/PhysRevB.98.174116

I. INTRODUCTION

Zirconium carbide is a hard, corrosion-resistant material, with a high melting point and metallic conductivity. The attractiveness of ZrC for aerospace and nuclear applications has been documented [1–4]. To support the experimental investigations of ZrC, particularly for safety critical applications, we seek to understand and predict some of the properties of this material at high temperature. In this regard, thermodynamic measurements are particularly challenging at temperatures approaching 3000 K or above, and theoretical predictions are few. Notable exceptions filling some of the gaps are the recent ultrahigh temperature measurements by Savvatimskiy *et al.*, and first-principles simulations by Duff *et al.* [5,6]. Nevertheless, even the currently most reliable phase diagram [7] is necessarily incomplete and based on empirical modeling, extrapolating from experimental data, which does not explicitly include data for point defects or their interactions [8].

Recent publications provide a hint that a ZrC crystal may contain a significant concentration of intrinsic carbon Frenkel defects at high temperature. Calculations by Kim *et al.* and Zhang *et al.* at zero temperature report low enthalpies of interstitial carbon formation [1,9], and the analysis of experiments conducted by Savvatimskiy *et al.* [6] near the melting point attribute heat capacity behavior at high temperature to possible Frenkel defects. In this work, we use temperature-dependent density-functional theory (DFT) calculations to address the possible formation of intrinsic defects, and deduce consequences thereof for thermal properties.

The plan of the paper is as follows. In Sec. II A we state technical parameters for numerical calculations, followed by the setting out of basic equations for the thermodynamic analysis in Sec. II B. Section III A details the discovery of defects by molecular dynamics, and describes our systematic search of the defect configuration space. In Sec. III B the calculated structures and stability of defects at 0 K is reported. Section III C discusses elementary thermal excitations in the defective crystal. Section III D reports some temperature-dependent properties, including Frenkel defect concentration, thermal expansion, heat capacity, and bulk modulus. Finally the effect of substoichiometry on Frenkel pair concentration is discussed. The Appendix contains supplementary details on the predicted ZrC properties and a derivation of the ideal solution model for the five Frenkel defects at variable carbon substoichiometry.

II. METHODS

A. Calculation

Langevin *NVT* molecular dynamics (MD) simulations were performed for five temperature-volume points up to the melting point on the ZrC thermal expansion curve [5]. MD simulations were run for 15 ps at each temperature-volume point, with a friction parameter of 0.1 THz and time step of 3 fs.

Periodic plane-wave density function theory (DFT) calculations were performed using the VASP software [10,11], with the local density approximation (LDA) exchange-correlation function [12]. The projector-augmented wave (PAW) method is used [13], with 4*s*- and 4*p*-Zr electrons included as valence

*t.mellan@imperial.ac.uk

TABLE I. Plane-wave kinetic energy cutoff and **k**-point sampling density for supercell calculations. Supercell size references diagonal expansion of basis vectors of the conventional unit cell of perfect ZrC.

Observable	E^{kin} (eV)	**k**-point grid	Supercell size
$U_0(V)$	700	$12 \times 12 \times 12$	$2 \times 2 \times 2$
$U_{\text{FS}}(V_0)$	700	$3 \times 3 \times 3$	$4 \times 4 \times 4$
$F_{\text{el}}(V,T)$	700	$12 \times 12 \times 12$	$2 \times 2 \times 2$
$F_{\text{ph}}(V)$	700	$6 \times 6 \times 6$[a]	$2 \times 2 \times 2$[a]
$E_{\text{MD}}(V,T)$	500	$2 \times 2 \times 2$	$2 \times 2 \times 2$

[a]For two unbound carbon Frenkel pairs it was necessary to increase the lattice expansion from $2 \times 2 \times 2$ to $4 \times 2 \times 2$, in order to obtain exact phonon frequencies at specific **q**-points. The **q**-point and **k**-point meshes were suitably adapted for these configurations.

states. The **k**-point sampling mesh and cutoff kinetic energies are chosen to obtain free energies converged to better than 1 meV/atom and 5 meV/defect. **k**-point mesh sampling and plane-wave cutoff values are summarized in Table I. The DFT crystal energy $U_0(V)$ and the phonon free energy $F_{\text{ph}}(V,T)$ were each calculated on a mesh of 11 volumes spanning the range 12.0 Å^3/atom to 14.7 Å^3/atom. $F_{\text{ph}}(V,T)$ was computed using quasiharmonic lattice dynamics as implemented in the PHONOPY code [14] with the direct method of calculating the dynamical matrix [15–17]. At each of the 11 volumes, sets of small displacements were applied. Each configuration required between 40 and 768 displacements depending on space group. The dynamical matrix was built from these forces [10–12,14]. For defect structures, we assumed that thermal expansion of the crystal can be modelled by a supercell with homogeneous isotropic principal axis strains. At each volume, internal coordinates were optimized until force changes were less than 10^{-6} eV/Å. Force calculations used first-order Methfessel-Paxton electron smearing with an electronic temperature of 0.1 eV [18].

The electronic free energy, $F_{\text{el}}(V,T)$, was calculated using the Mermin finite-temperature formulation of DFT [19], on a mesh of ten temperatures and eight volumes, sampled between $V_{\text{eq}}(T = 0\ \text{K})$ and $V_{\text{eq}}(T = 3800\ \text{K})$. Electron states are self-consistent to within 10^{-7} eV/atom. The 64 atom supercell used contains 512 electrons, for which 384 bands were sufficient to span all states with significant partial occupation up to the melting point.

B. Analysis

We calculate the Helmholtz free energy

$$F = -k_{\text{B}} T \ln Z,$$

as a sum of three terms

$$F(V,T) = U_0(V) + F_{\text{ph}}(V,T) + F_{\text{el}}(V,T). \tag{1}$$

U_0 is the total energy of static crystal configurations, F_{ph} the vibrational free energy, and F_{el} the contribution of single-electron thermal excitations as described in the Mermin functional.

The calculated free energies are fitted by third-degree polynomials,

$$F(V,T) = \sum_{jk} a_{jk} V^j T^k, \tag{2}$$

with $j \geqslant 0$, $k \geqslant 1$ and $j + k \leqslant 3$.

The Helmholtz free energy F is Legendre transformed to the Gibbs free energy G for calculating thermodynamic quantities at constant external pressure p:

$$G(p,T) = \min_V [F(V,T) + pV]. \tag{3}$$

The volume minimization is performed on a mesh of temperatures separated at 2 K intervals.

For intrinsic defect i in a stoichiometric $2 \times 2 \times 2$ supercell, G_i is used to calculate the defect formation energy:

$$\Delta G_i^{2\times2\times2} = G_i^{2\times2\times2} - G_{\text{perfect}}^{2\times2\times2}. \tag{4}$$

The spurious interaction between the defect and its periodic images, both electronic and due to the overlapping strain fields, is accounted for with a finite-size energy correction,

$$\Delta G_i^{\text{bulk}} = \Delta G_i^{2\times2\times2} + U_{i,\text{FS}}(V_0). \tag{5}$$

The finite-size correction $U_{i,\text{FS}}$, is estimated from calculations at the zero-temperature equilibrium volume,

$$U_{i,\text{FS}}(V_0) = \lim_{n\to\infty} U_i^{n\times n\times n}(V_0) - U_i^{2\times2\times2}(V_0), \tag{6}$$

where $U_i^{n\times n\times n}(V_0)$ is the energy to form a defect in a $n \times n \times n$ supercell. To estimate $U_{i,\text{FS}}(V_0)$ in the limit of noninteracting periodic images, the defect energy is calculated for supercell sizes ranging from $2 \times 2 \times 2$ ($Zr_{32}C_{32}$) to $4 \times 4 \times 4$ ($Zr_{256}C_{256}$), and linearly extrapolated to the $1/n = 0$ dilute limit.

The equilibrium concentration of intrinsic defects has been calculated using the dilute-limit ΔG_i^{bulk} with an ideal solution model. The model assumes a partition function of the form

$$Z = m_2^{N_2} m_3^{N_3} \frac{N!}{(N - N_1 - N_2 - 2N_3)!\,(N_1 + N_3)!\,N_2!\,N_3!},$$

where m_i are degeneracies and N_i are defect numbers, indexed $i = 1, 2, 3$ for vacancies, bound pair Frenkels and unbound pair Frenkels respectively. Z gives

$$n_2 = (1 - n_1 - n_2 - 2n_3)\, m_2 \exp\left(-\frac{\Delta G_2}{T}\right),$$

and

$$n_3 = \frac{(1 - n_1 - n_2 - 2n_3)^2}{(n_1 + n_3)}\, m_3 \exp\left(-\frac{\Delta G_3}{T}\right).$$

for bound and unbound Frenkel pair concentrations. Model derivation and additional details in the Appendix.

III. RESULTS

A. Discovery of defects

1. Molecular dynamics

With density functional theory (DFT) we first performed *ab initio* molecular dynamics (AIMD) simulations for stoichiometric ZrC. Although the time scales accessible in AIMD

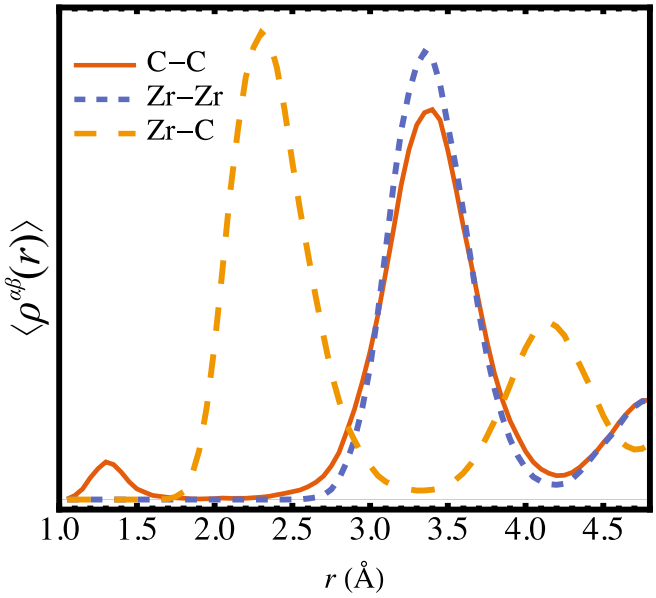

FIG. 1. Time-averaged pair correlation function, $\langle \rho^{\alpha\beta}(r) \rangle$ in Eq. (8), estimated from *ab initio* MD at the melting point $T_m = 3700$ K.

simulations are typically insufficient to determine defect statistics such as bound pair lifetimes, even short runs of 15 ps can provide insight into defect behavior. Trajectories were analyzed using equal-time spatial pair correlation function defined as follows:

$$\rho^{\alpha\beta}(r,t) = \frac{1}{N_\alpha} \sum_{i,\, j \neq i} \left\langle \delta\left(r - \left|r_i^\alpha - r_j^\beta\right|\right) \right\rangle, \tag{7}$$

where $\alpha \in \{Zr, C\}$ and $\beta \in \{Zr, C\}$. The time argument is specified in $\rho^{\alpha\beta}(r,t)$ as we do not suppose the thermodynamic limit for our small ensemble simulations.

Near the melting point, carbon atoms are occasionally observed to hop spontaneously from $(\frac{1}{2}\ \frac{1}{2}\ \frac{1}{2})$ perfect Wyckoff b sites, with high-symmetry and octahedral coordination, to low-symmetry interstitial sites. Site-resolved pair correlation functions show that newly formed carbon interstitials do not immediately leave sites that are nearest neighbor to the vacancy they have created. We therefore refer to the resulting defect as a bound pair carbon Frenkel defect.

The time-averaged correlation functions,

$$\langle \rho^{\alpha\beta}(r) \rangle = \frac{1}{\tau} \int dt\ \rho^{\alpha\beta}(r,t) \tag{8}$$

are shown for stoichiometric ZrC at the melting point in Fig. 1. The distinctive carbon-carbon peak at the small separation of $r = 1.3$ Å signifies interstitial carbon in ZrC. The width of the peak suggests the interstitial carbon is sufficiently thermally excited to move between multiple coordinations (which have a range of C-C bond lengths). Examining this behavior using AIMD simulations requires significant computational resources. To aid sampling of the interstitial configuration space, interstitial dynamics has been biased to prohibit the recombination of interstitial and vacancy.

To bias interstitial dynamics a hydrogen atom is placed and frozen in position at the vacant carbon site. At the melting temperature, the interstitial is found to exchange between multiple sites within the vacancy nearest-neighbor (nn) coordination shell. Within 10 ps, the interstitial is observed to begin diffusing, hopping away from vacancy-nn coordination. Beyond the vicinity of the vacancy-nn, the displaced carbon can hop between lattice interstitial sites, or switch places with a perfect-site carbon. In AIMD simulations we cannot access fine-grained diffusion statistics, but note that hopping behavior between distinct sites is quite clearly observed on the picosecond time scale.

The carbon Frenkel pairs observed in AIMD at the melting point are found to be metastable at low temperature. This is confirmed by selecting MD configurations at random, and quenching by steepest descent to $T = 0$ K. The Frenkel interstitial tends to relax to a C-C-C trimer unit, with a bond angle of 127° and C_{2v} symmetry. The trimer is found to be stable across volume dilations ranging from at least −5% to +16% under homogeneous principal axis strains.

2. Systematic search for Frenkel pairs

In addition to the carbon trimer of C_{2v} symmetry, identified from quenched AIMD snapshots, we have systematically searched for other carbon Frenkel defect configurations with distinct symmetry. 1331 initial Frenkel configurations were considered, each corresponding to a different interstitial position. The interstitial positions were distributed on a uniform grid in a symmetry-reduced wedge of the defective $2 \times 2 \times 2$ supercell with other atoms fixed in their perfect lattice sites. Each configuration provided a starting point for a geometry optimization. Optimized configurations were subsequently analyzed in terms of energy and symmetry to identify distinct metastable Frenkel configurations.

In the relaxation of the 1331 initial Frenkel configurations, forces were finely optimized to better than 10^{-6} eV/Å. This was necessary to prevent relaxations becoming trapped in flat, high-symmetry regions of the defect configuration space that are not quite local minima. The high-accuracy relaxations provide data from which we identify two bound and three unbound interstitial-vacancy pairs that are stable at the equilibrium volume. If $d(C_{\text{int}} - C_{\text{vac}}) < a/\sqrt{2}$ the vacancy-interstitial pair is classified as bound, and if $d(C_{\text{int}} - C_{\text{vac}}) > a/\sqrt{2}$ the Frenkel pair is said to be unbound.

3. Defect structures

Of the five defects considered as bound (B) or unbound (U) Frenkel pairs, the carbon atoms involved are further classified as dimer, trimer, or tetramer, denoted by a subscript suffix. For each configuration, bound-dimer (B_2), bound-trimer (B_3), unbound-dimer (U_2), unbound-trimer (U_3), unbound-tetramer (U_4), the energetic ordering at the zero-temperature equilibrium volume is as follows:

$$\text{perfect} < B_3 < B_2 < U_3 < U_2 < U_4.$$

Formation energies are listed in Table IV, each defect structure is pictured in Fig. 2, and features of the defect geometries such as bond lengths and point symmetries are listed in Table II.

Note, at the equilibrium volume, the U_3 configuration is an angular C-C-C unit, but the linear C-C-C configuration, U_3^{lin},

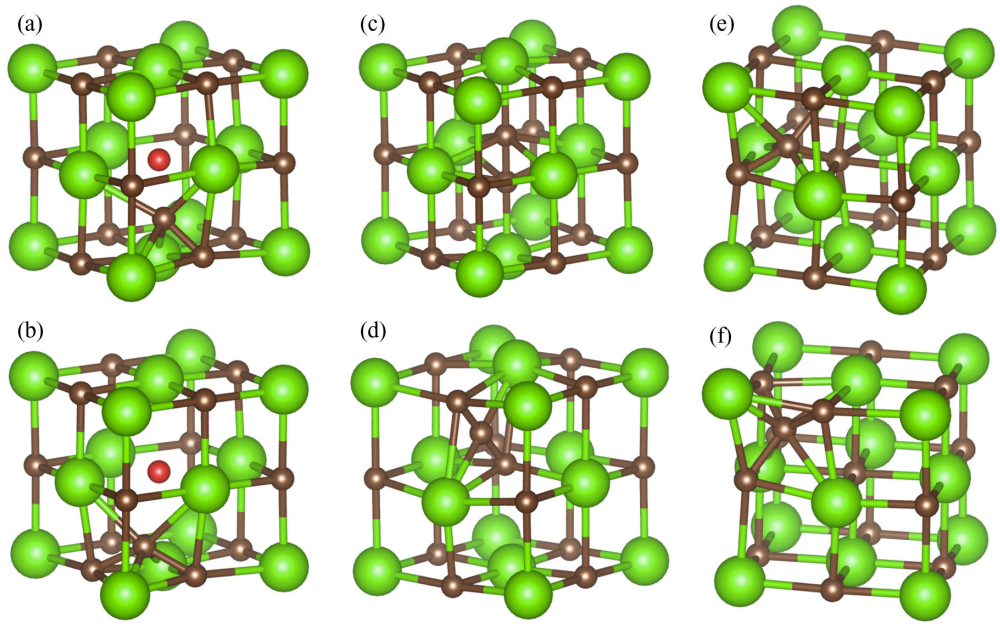

FIG. 2. For each Frenkel pair, the eighth of the supercell that contains the interstitial atom is visualized [20]. Carbon atoms are colored brown, zirconium atoms green, and the vacant carbon site is highlighted red for bound pair defects. Defect labels are: (a) B_2 bound dimer, (b) B_3 bound trimer, (c) U_2 unbound dimer, (d) U_3^{lin} unbound linear trimer, (e) U_3 unbound trimer, and (f) U_4 unbound tetramer.

is stabilised at sufficiently large lattice expansion. Both are shown in Fig. 2.

B. Electrons and phonons

1. Lattice vibrations with defects

Phonon densities of states (DOS) are shown as a function of frequency and volume dilation in Fig. 3. Typically vibration frequencies soften with lattice expansion. For example the mean Grüneisen parameter ($\gamma = -\frac{\partial \ln \bar{\omega}}{\partial \ln V}$) for perfect ZrC is $\gamma^{\text{perf}} \approx 1.5$ at low temperature, increasing to $\gamma^{\text{perf}} \approx 2$ at high temperature. A notable feature of the perfect ZrC phonon DOS is the obvious gap in frequencies. For each density of states, below the gap 98.6% of the squared amplitude is on Zr sites, and above the gap 98.6% is on C sites.

Carbon Frenkel defects can be identified in the phonon DOS (Fig. 3) from the distinctive patterns of high-frequency vibrations associated with the interstitial carbon. The patterns shown may provide a useful spectroscopic fingerprint to experimentally identify Frenkel pairs in the future.

The most stable defect configuration at $T = 0$ K is B_3 (see Table IV), for which the phonon DOS is shown in Fig. 3(c). The B_3 defect states comprise localized carbon vibrational frequencies with one mode red-shifted and three modes blue-shifted enough to lie outside the band of bulk carbon frequencies. The red-shifted defect mode, clearly evident in the gap between the bulk carbon and zirconium frequencies, is due to rigid C-C-C translation. For the blue-shifted modes, the highest-frequency vibration is an asymmetric stretch. The other two blue-shifted local modes are types of symmetric stretches, which are distinguished by the motion of the interstitial relative to the local environment as in or out of the C-C-C plane.

To quantify the high degree of localization for these vibrations, consider the highest-frequency defect state in Fig. 3(c). For this asymmetric stretch mode, 60.1% of the motion

TABLE II. This table reports stable carbon Frenkel pair configurations found in ZrC. Defect configurations are labeled bound (B) or unbound (U), with C coordination subscripts. Orientations are specified by angle brackets which denote the families of directions for the C_{i}-C_{nn} bond in the basis of the direct unit cell lattice. Orientation indices given are the lowest that provide accuracy to within 5% of the exact orientations. The point group refers to the interstitial-carbon nearest-neighbor unit. Multiplicity m counts the degeneracy of the interstitial carbon, with respect to vacancies for bound pairs, and per perfect carbon site for unbound pairs. Bond angles and lengths are between interstitial-carbon and carbon nearest-neighbors.

Config.	Description	Orientation	Point group	Multiplicity, m_{i}	Angle, C_{nn}-C_{i}-C_{nn}(°)	Length, C_{nn}-C_{i} (Å)
B_2	bound dimer	⟨332⟩	$D_{\infty h}$	24	–	1.411
B_3	bound trimer	⟨654⟩	C_{2v}	24	126.7	1.506
U_2	unbound dimer	⟨100⟩	$D_{\infty h}$	3	–	1.411
U_3	unbound trimer angular	⟨553⟩	C_{2v}	12	135.9	1.459
U_3^{lin}	unbound trimer linear	⟨110⟩	$C_{\infty v}$	6	179.4	1.376
U_4	unbound tetramer	⟨322⟩	C_{3v}	8	117.4	1.586

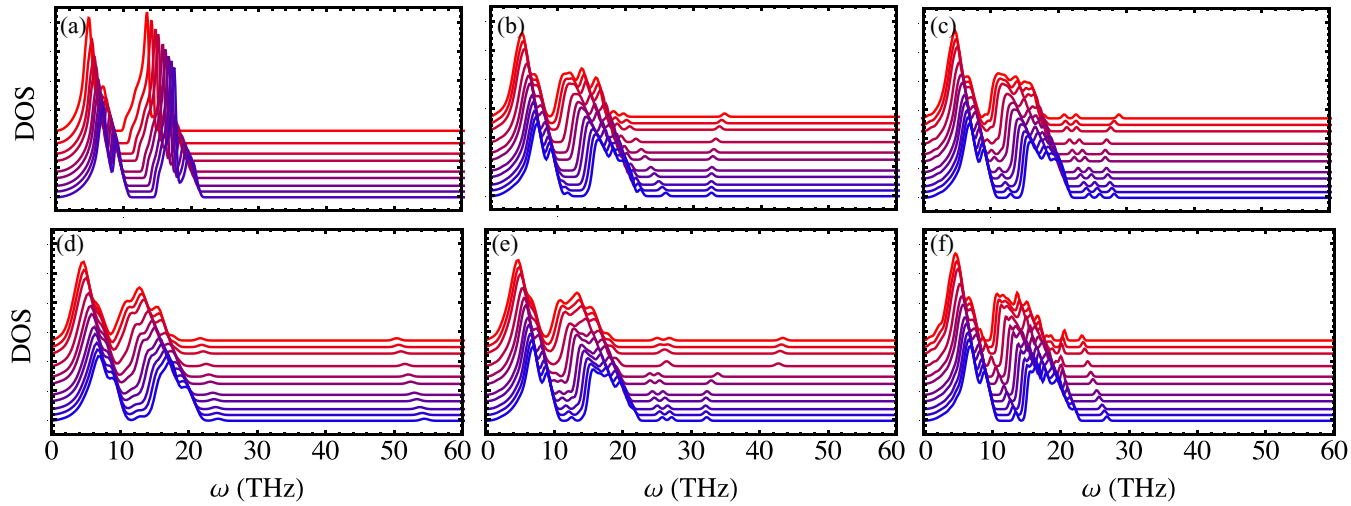

FIG. 3. Phonon density of states for: (a) perfect ZrC, (b) B_2 bound dimer, (c) B_3 bound trimer, (d) U_2 unbound dimer, (e) U_3 unbound trimer, (f) U_4 unbound tetramer. Thermal expansion increases from blue to red, along the sequence of volumes {11.96, 12.16, 12.36, 12.63, 12.85, 13.22, 13.47, 13.83, 14.26, 14.48, 14.70} Å^3/atom. To highlight Grüneisen behavior, consecutive densities of states are up-shifted proportional to dilation.

projects onto the interstitial, and 19.3% projects onto each of the two interstitial nearest neighbors. Only the remaining 1.3% is not localized on the immediate C-C-C unit. For B_2, shown in Fig. 3(b), the blue-shifted defect frequencies involve a C-C stretching mode, which has the highest frequency, and second mode in which the interstitial rocks about a near-static carbon neighbor. The frequency-volume dependence of the rocking mode mirrors the Grüneisen parameter of bulk frequencies, softening with strain, but the stretching mode anomalously increases in frequency with lattice expansion.

The U_2 phonon states in Fig. 3(d) are further worth mentioning. The U_2 DOS shows one remarkably high-frequency peak at $\omega \approx 54$ THz. This vibration is due to stretching of the C-C dimer. The other blue-shifted defect mode is a dimer translation parallel to the bond orientation. The red-shifted defect frequencies, which overlap into the bulk carbon range, are due to C-C partial rotation in one instance, and in another due to dimer translation orthogonal to the C-C bond.

U_3 in Fig. 3(e) is also notable for the phase transition in strain evident via the Grüneisen discontinuity at large dilation. The transition occurs between crystal volume 13.5 and 13.8 Å^3/atom and lifts the trimer point group symmetry from angular C_{2v} to linear $C_{\infty v}$. This change yields another unusually stiff mode at 43 THz shown in Fig. 3(e), which is due to asymmetric stretching of the C-C-C unit. Two other high-frequency localized modes exist, which have the same Grüneisen parameters below the transition. At the transition, the lower-frequency mode changes Grüneisen sign, and begins increasing in frequency. This gives the appearance of a degeneracy at the eighth and ninth volumes in Fig. 3(e), but closer inspection reveals the modes are not degenerate. In Fig. 3(e) we also note there are two low frequency localized modes in the gap evident below the transition. Above the transition there are still two localized modes at the gap, but they are not clearly observable in the total DOS plot due to proximity to bulk modes.

For U_4 in Fig. 3(f), the stiffest defect mode is due to the carbon interstitial stretching against its three carbon nearest-neighbors. The observable red-shifted defect mode, between the bulk carbon and zirconium bands, is due to the rigid translation of the C_4 unit which is made up of the interstitial and it's three C nearest-neighbors.

Harmonic interatomic forces and vibration frequencies are related as

$$|\mathbf{\Phi}| = |\mathrm{M}| \prod_i \omega_i^2. \tag{9}$$

In this expression the force constant matrix determinant $|\mathbf{\Phi}|$ is equated with the product of the diagonal mass matrix entries $|\mathrm{M}|$ and the squared frequencies ω_i^2.

The defective to perfect ratio $|\mathbf{\Phi}'|/|\mathbf{\Phi}|$ is a useful indicator of bond stiffness. In particular for stoichiometric defects when $|\mathrm{M}| = |\mathrm{M}'|$ the force determinant ratio is a useful single-valued measure of the defect-induced frequency redistribution. The ratio can be expressed as a density of states difference integral

$$|\mathbf{\Phi}'|/|\mathbf{\Phi}| = \exp \int d\omega \, [g'(\omega) - g(\omega)] \ln \omega, \tag{10}$$

which is how we have calculated the ratio in practice in this work. It is also directly related to the classical excess vibrational entropy of the Frenkel defect by

$$S' - S = -\ln \sqrt{|\mathbf{\Phi}'|/|\mathbf{\Phi}|}.$$

If $|\mathbf{\Phi}'|/|\mathbf{\Phi}| < 1$ we infer net defect-induced crystal softening, else vice versa. For Frenkel defects in ZrC we observe $|\mathbf{\Phi}'|/|\mathbf{\Phi}| \ll 1$, indicating stoichiometric defects reduce crystal stiffness. This occurs despite the high-frequency vibrations of Frenkel defects (visible in Fig. 3), that arise from locally stiffened interstitial carbon-carbon bonds, as explained in what follows.

The values of S'-S reported in Table III are positive, which agrees in sign with Frenkel pair entropies reported for other

TABLE III. Defective to perfect force determinant ratios $|\mathbf{\Phi}'|/|\mathbf{\Phi}|$ and formation entropy for each Frenkel pair. Values are isochoric at the perfect volume $V_0^{\text{perf}} = 12.843$ Å/atom. Entropies resolved to cation and metal contributions. k_B/defect entropy units.

Configuration	$\lvert\mathbf{\Phi}'\rvert/\lvert\mathbf{\Phi}\rvert$	$S' - S$	$S'_{Zr} - S_{Zr}$	$S'_C - S_C$
B_2	0.09	1.18	2.16	−0.97
B_3	0.24	0.72	2.13	−1.41
U_2	0.01	2.29	2.45	−0.16
U_3	0.06	1.40	2.53	−1.13
U_4	0.08	1.26	2.46	−1.20

materials [21–24]. The unbound defects have larger vibrational entropies than bound defects, which is also consistent with reports for other materials, e.g., the Frenkel pairs in In_2O_3 reported by Walsh *et al.* [22].

S'-S at fixed perfect-crystal volume ranges from 0.7–2.3 k_B depending on the defect. Partial S'-S contributions from carbon and zirconium in Table III show S'-S is positive because the Zr-character modes soften more than the carbon-type vibrations increase in frequency due to the localized interstitial frequencies. An early Green's function analysis of Frenkel pairs in CaF_2 by Gillan and Jacobs made a similar partition of the defect entropy [21]. The conclusions they drew were analogous—Frenkel defect entropy S'-S is net positive, despite the locally negative entropy of the stiffened interstitial vibrations.

2. Defect electronic characterization

Our DFT calculations predict that perfect ZrC has a density of states at the Fermi energy of DOS(ϵ_F) = 0.13 electron states/eV per atom. This value is similar to early estimates by Ihara *et al.* [25] with 0.09 states/eV per atom, and Borukhovich and Geld [26] with 0.1 states/eV per atom, and more recent LDA (GGA) calculations by Arya and Carter [27] with 0.112 (0.129) states/eV. Absolute computed values depend somewhat on technical parameters. For example we observe a 5% variation in DOS(ϵ_F) on converging unit cell k-points between 4 × 4 × 4 and 40 × 40 × 40, +7% change increasing $T_{el} = 0.1$ eV to $T_{el} = 0.2$ eV, +2% change from Fermi-Dirac smearing to Methfessel-Paxton, and +12% increase from GGA to LDA at fixed volume. Given these sensitivities, we next consider trends with defect type and thermal expansion rather than absolute values.

The value of DOS(ϵ_F) is modified by the presence and type of the carbon Frenkel defect in the crystal. A feature common to each defect is the tendency to increase DOS(ϵ_F) compared to perfect ZrC. Compared to 0.13 states/eV/atom in perfect ZrC, Frenkel defects increase DOS(ϵ_F) by between +0.02 states/eV/atom for U_3 and +0.12 states/eV/atom for U_2.

The value of DOS(ϵ_F) in a transition metal can become larger or smaller with increasing Wigner-Seitz radius, for example, this has been reported by Pettifor for the 4*d* series [28]. In ZrC we find the precise dependence of DOS(ϵ_F) on volume expansion varies depending on the specific defect configuration, illustrated in Fig. 4.

As lattice dilation and the insertion of defects both tend to increase the value of DOS(ϵ_F), electron entropy will tend to stabilize defects. The distribution of DOS(ϵ) for each crystal configuration has a distinctive energy dependence (see Fig. 4). At high temperatures a first-order Sommerfeld expansion will be inadequate beyond qualitative inferences. Quantitative predictions including electronic defect free energies from the Mermin functional are given subsequently.

C. Defect thermodynamics

1. Enthalpy and entropy

The B_3 Frenkel defect is the most energetically stable configuration at 3.2 eV/defect, followed by B_2 at 3.7 eV/defect. Unbound pairs are less stable, costing between 4.3 and 4.5 eV/defect to introduce to the lattice. The full set of values at $T = 0$ K is listed in Table IV, and shown as a function of temperature at ambient pressure in Fig. 5. The defect formation enthalpies, $\Delta H = H^{\text{defect}} - H^{\text{perfect}}$, show variations of a few tenths of an eV over 3000 K. The relatively weak temperature dependence is due to partial cancellation of vibrational and electronic contributions. To see this consider the bound dimer enthalpy $\Delta H(B_3)$ as a typical example. Between 0 K and 3000 K, the electronic part increases by $\Delta H_{el}(B_3) = 0.14$ eV/defect, and quasiharmonic part decreases by $\Delta H_{ph}(B_3) = -0.25$ eV/defect. Overall change is modest at $\Delta H(B_3) = -0.12$ eV/defect, as evident in Fig. 5.

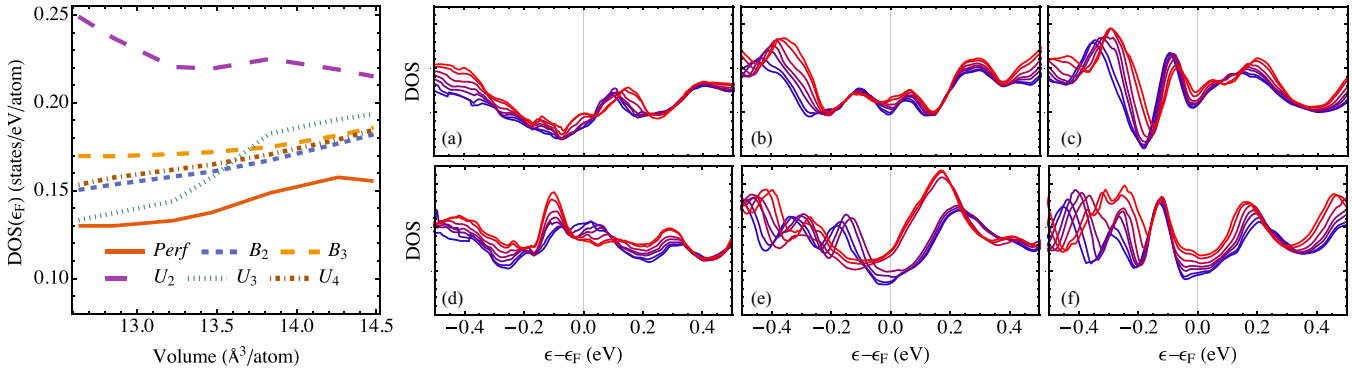

FIG. 4. Electron densities of states (DOS). Left: DOS at the Fermi level versus crystal expansion. Right: DOS versus energy, with thermal expansion increasing from blue to red. (a) perfect ZrC, (b) B_2 bound dimer, (c) B_3 bound trimer, (d) U_2 unbound dimer, (e) U_3 unbound trimer, (f) U_4 unbound tetramer. Note, electron DOS is provided for on the wider scale of $-6 \leqslant \epsilon - \epsilon_F \leqslant 6$ in the Appendix.

TABLE IV. Defect formation energy ΔU ($\Delta U = \Delta U_0 + \Delta U_{ZP} + U_{FS}$) and zero-point energy difference ΔU_{ZP}.

Configuration	ΔU (eV/defect)	ΔU_{ZP} (eV/defect)
B_2	3.734	−0.031
B_3	3.247	−0.016
U_2	4.436	−0.042
U_3	4.335	−0.027
U_4	4.441	−0.030

B_3 has the smallest ambient pressure formation entropy and U_2 has the largest, as seen in Fig. 5. The ordering of defect entropies agrees with the rudimentary estimates in Table III computed from fixed-perfect-volume force-constant determinants, though the ambient pressure values are larger.

2. Gibbs energy of defect formation

The Gibbs energy of defect formation is shown in Fig. 6 up to 3000 K (above this temperature anharmonic thermodynamic contributions become considerable in ZrC) [5]. Thermally excited electrons and phonons can reduce the energy to form a Frenkel defect by more than 1 eV over the interval 0–3000 K. This is mostly due to phonons but the electron contribution gains relative importance with temperature. In terms of the Gibbs energy of defect formation, zero-point effects are negligible. This is observable in Fig. 6 and Table. IV.

3. Bulk modulus

We estimate the isothermal bulk modulus as

$$K_T = -V\frac{\partial^2 G}{\partial V^2}. \tag{11}$$

K_T is shown in Fig. 7, and specific values are reported in Table V.

K_T is known experimentally for ZrC from pulsed-ultrasonic measurements by Chang and Graham, who report $K_{300}^{exp} = 223$ GPa for $ZrC_{0.94}$. At 300 K, we predict $K_{300}^{perfect} = 236$ GPa, and $K_{300}^{defect} \approx 219$–$227$ GPa depending on the type

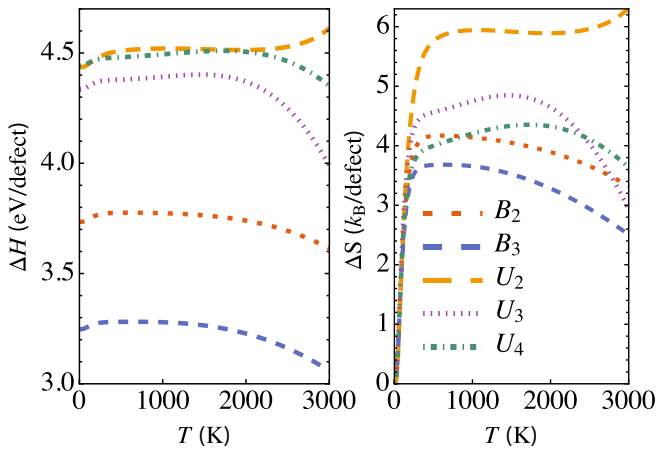

FIG. 5. Ambient pressure formation energy $\Delta H = H^{defect} - H^{perfect}$ and entropy $\Delta S = S^{defect} - S^{perfect}$. Frenkel ZrC has one defect per supercell.

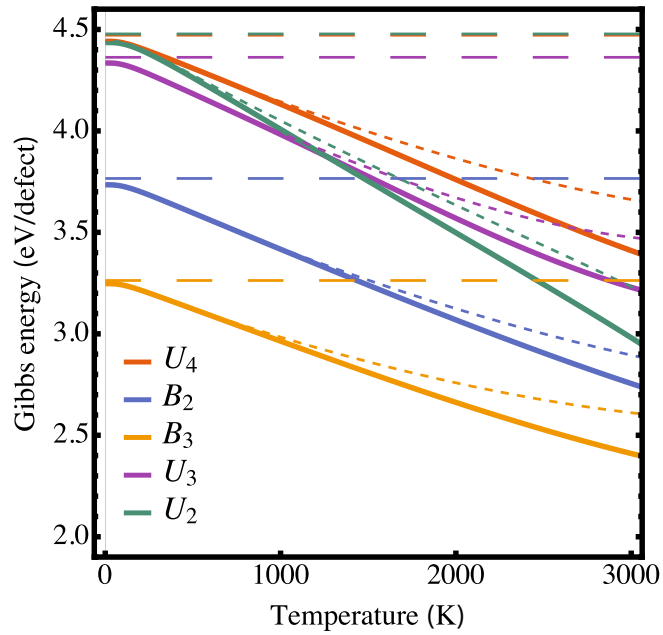

FIG. 6. Defect Gibbs formation energy [Eq. (5)] for each defect type. Solid includes quasiharmonic and electronic contributions; short-dashed includes quasiharmonic; and long-dashed is the zero-temperature formation energy without zero-point contributions.

of Frenkel defect present in the simulation cell. The defect reductions in K_T are between 5–10 % at the Frenkel concentration of one defect by supercell (1/32 C at. %). Frenkel-induced K_T variation is relevant to ZrC applications in high-radiation and -temperature environments. ZrC is radiation tolerant and has a relatively low neutron scattering cross section $\sigma_{ZrC} \approx 0.2\,\sigma_{ZrAlloy}$) [29,35,36], but there is reportedly less known about ZrC for fuel clad design that comparable materials such as SiC [35,37,38]. First-principles data on Frenkel-induced changes to structural parameters is therefore likely useful for sensitivity analyses in multiphysics simulations of accident tolerant fuel materials [39–42].

The K_0 value we predict for perfect ZrC differs from other computational studies by 10–20 GPa [29–31,33]. While most studies use the PBE GGA functional, we use the LDA exchange correlation. Our choice of the LDA functional has been motivated by the adequate performance of LDA and poor performance of PBE at high temperature for ZrC reported by Duff *et al.* [5].

4. Heat capacity

The ambient-pressure isobaric heat capacity,

$$C_P = -T\frac{\partial^2 G}{\partial T^2} \tag{12}$$

$$= C_V + T\frac{\partial S}{\partial V}\frac{\partial V}{\partial T}, \tag{13}$$

is shown for perfect ZrC in Fig. 7, along with the excess defect contribution $\Delta C_P(T) = C_P^{defect}(T) - C_P^{perfect}(T)$ associated with forming a single defect.

The low-temperature peak arises from the differential temperature occupation of the perfect and defect crystal phonon spectra. Low-frequency modes are softer in the defective

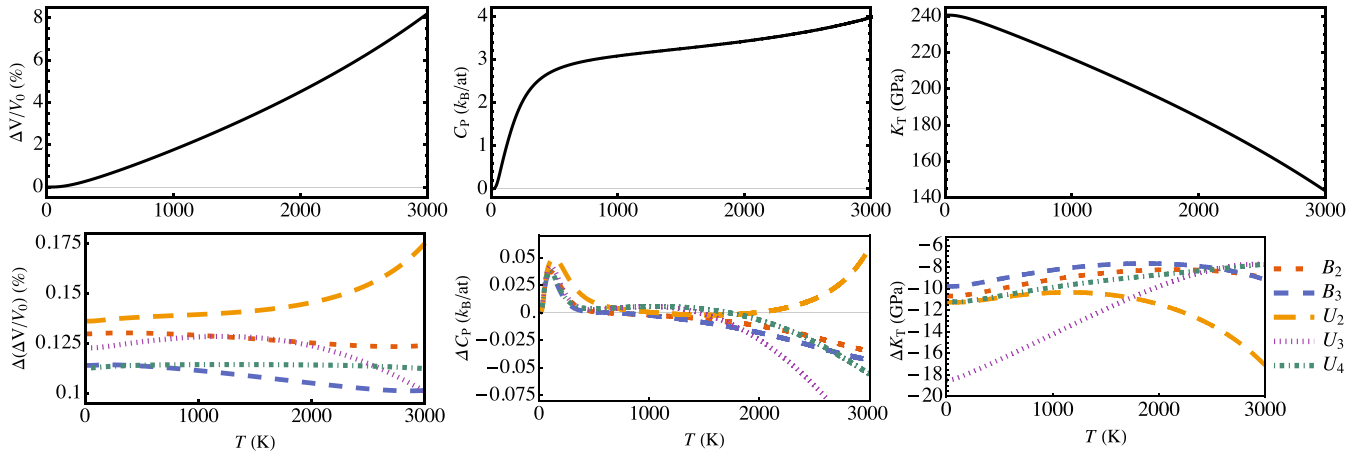

FIG. 7. Top, left to right: Thermal volume expansion ($\Delta V/V_0$), isobaric heat capacity (C_P), and isothermal bulk modulus (K_T) for perfect ZrC. Bottom: The defective minus perfect difference, $\Delta\mathcal{O} = \mathcal{O}^{\text{defect}} - \mathcal{O}^{\text{perfect}}$, for each quantity. The defective ZrC here has one Frenkel defect per supercell.

lattice compared to the perfect crystal. As temperature increases, the defect crystal heat capacity increases more than perfect ZrC resulting in the peak. As the crystal approaches the Debye temperature, quantum effects in the heat capacity fall off and the difference $\Delta C_P(T)$ recedes. We emphasise the low-temperature bump is not an isobaric effect, i.e., it is not due to the second term in Eq. (13). It is also present in a plot of the constant volume equivalent $\Delta C_V(T)$.

Our heat capacity predictions can be considered in the context of measurements by Savvatimskiy *et al.* [6], which show a steep increase in specific heat by $\times 4$ near T_m, tentatively attributed to carbon Frenkel pair defects. Direct comparison is somewhat limited because their measurements are made on a sample undergoing fast heating from 2500–5000 K while we predict equilibrium thermodynamics up to 3000 K, however, we can confirm that at 3000 K the calculated population of Frenkel defects is already sufficient to modify the heat capacity by $\Delta C_P = 0.05$ k_B/atom. This value is small compared to the experimental enhancement at T_m, but at higher temperatures we speculate the ΔC_P from Frenkel defects will be much greater due to the exponentially increasing number of defects and the increasing effects of anharmonicity. As the electronic contribution to the heat capacity at T_m is known to be 0.5 k_B/atom [5], which is only a small fraction of the measured C_P enhancement, and ZrC is unusually capable of supporting Frenkel defects, it seems plausible that structural excitations are the source of the measured heat capacity divergence. However, we are cautious in asserting this as our calculated ΔC_P can be positive or negative depending on the Frenkel defect type (whereas the measured enhancement is strongly positive). Furthermore the inclusion of anharmonic effects required to calculate C_P at T_m is beyond the scope of this work.

5. *Thermal expansion*

The isotropic volume expansion $\frac{\Delta V}{V}$ is found from the volume that minimizes the Gibbs free energy at each temperature. It is shown for each configuration in Fig. 7, at a concentration of one defect per 64 atom supercell ($n_{\text{fp}} = 3$ C at. %), and values are listed in Table VI. The volume expansion induced by one carbon Frenkel defect in the supercell is approximately 0.12%, with weak dependence on temperature. We consider in the following sections the effect of a thermal population of defects.

TABLE V. Isothermal bulk moduli in units of GPa for perfect and defective ZrC. Frenkel ZrC has one defect per supercell. Selected calculated [29–33] and measured [34] values are included.

Configuration	K_0	K_{300}	K_{1000}	K_{3000}
perfect	240.7	236.2	216.7	143.6
B_2	230.0	225.8	207.6	134.6
B_3	230.9	226.8	208.4	134.4
U_2	229.5	225.1	206.3	126.4
U_3	222.2	218.8	202.5	135.9
U_4	229.5	225.2	206.8	135.9
ZrC (PBE)	232.2 [29], 219 [30], 232 [31,32], 234 [33]	–	–	–
$ZrC_{0.94}$(ultrasonic)	–	223 [34]	–	–

TABLE VI. Volume for perfect and defective ZrC at 0 K, 300 K, 1000 K, and 3000 K. Frenkel ZrC has one defect per supercell. Units of Å^3/atom

Configuration	V_0	V_{300}	V_{1000}	V_{3000}
perfect	12.706	12.740	12.931	13.749
B_2	12.836	12.870	13.060	13.873
B_3	12.820	12.854	13.042	13.850
U_2	12.843	12.877	13.070	13.924
U_3	12.829	12.864	13.059	13.850
U_4	12.819	12.854	13.045	13.861
ZrC (PBE)	12.903 [32] 12.887 [33]	–	–	–
$ZrC_{0.94}$(exp.)	–	12.973 [6]	–	–
$ZrC_{0.95}$(exp.)	–	12.928 [34]	–	–

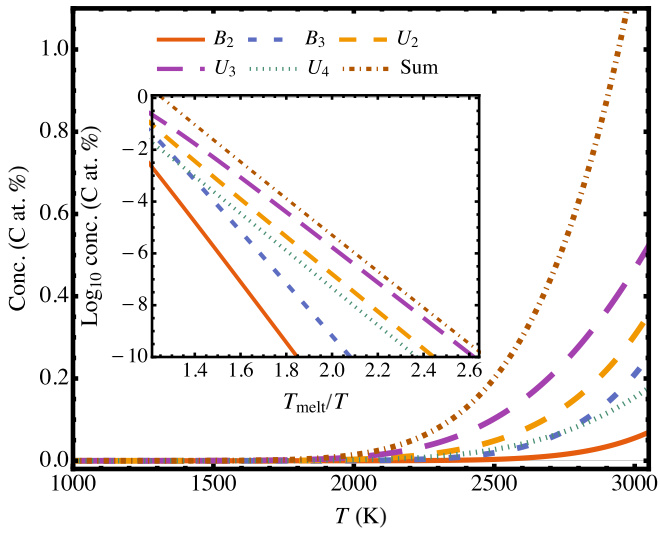

FIG. 8. Frenkel pair concentration. Log scale inset.

6. Defect concentration

n_{fp} is shown in Fig. 8 between 1000 and 3000 K, calculated with the ideal solution model. Details are provided in Appendix A. n_{fp} ranges from 0.01% at 2000 K (0.54 T_{m}) to 1.2 C at.% at 3000 K (0.81 T_{m}), where the experimental melting point is $T_{\mathrm{m}} = 3700$ K. We are unaware of any reports of such high concentrations of thermally induced self-interstitials in any material hundreds of degrees below the melting point. Recent evidence, both experimental and with molecular dynamics, has indicated the existence of thermally induced self-interstitials in aluminium, but only within 2–4 K of T_{m} [43], and at a concentration two or three times below that of the thermally induced vacancies. Since we are dealing here with a compound, the concept of thermally induced vacancies is not directly relevant; in the case of ZrC any concentration of carbon vacancies not associated with Frenkel defect formation is associated with nonstoichiometry. In practice, the ZrC lattice structure supports a high level of carbon deficit, manifest as vacancies on the carbon sublattice. The law of mass action dictates that such constitutional vacancies will reduce the concentration of unbound interstitials. Figure 9 shows the calculated effect of substoichiometry on the Frenkel defect population at 3000 K. Some specific values are also listed in Table VII.

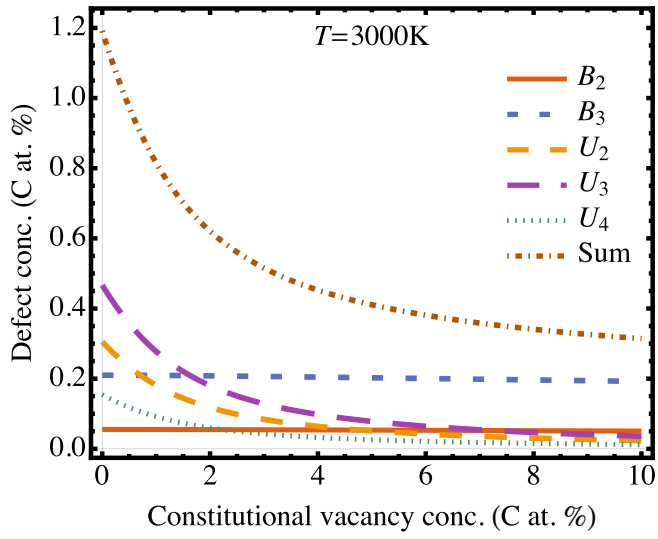

FIG. 9. Coupling of equilibrium Frenkel defect concentration at 3000 K to carbon substoichiometry. Constitutional carbon vacancies weakly suppress bound pair defects and strongly suppress unbound pairs.

TABLE VII. Frenkel pair concentration. Concentrations measured in C at. %.

T (K)	$n_{\mathrm{vac}}^{\mathrm{C}}$	$n_{\mathrm{fp}}^{\mathrm{bound}}$	$n_{\mathrm{fp}}^{\mathrm{unbound}}$	$n_{\mathrm{fp}}^{\mathrm{total}}$
	0	5×10^{-4}	0.01	0.01
	2	5×10^{-4}	9×10^{-5}	6×10^{-4}
2000	5	5×10^{-4}	4×10^{-5}	5×10^{-4}
	10	5×10^{-4}	2×10^{-5}	5×10^{-4}
	0	0.02	0.18	0.20
	2	0.02	0.02	0.04
2500	5	0.02	6×10^{-3}	0.03
	10	0.02	3×10^{-3}	0.02
	0	0.27	0.93	1.19
	2	0.26	0.36	0.62
3000	5	0.26	0.16	0.41
	10	0.24	0.07	0.31

The exceptional population of carbon Frenkel defects is explained by the following five points:

(i) ZrC supports at least five symmetry-inequivalent Frenkel-pair types, $\{B_2, B_3, U_2, U_3, U_4\}$.

(ii) Interstitial carbon tends to occupy low-symmetry sites. The associated multiplicities are listed in Table II.

(iii) Frenkel pairs increase the electronic density of states at the Fermi level.

(iv) Frenkel pairs expand the lattice, with a net softening of vibration frequencies.

(v) ZrC remains crystalline to an unusually high melting temperature. Configurational, electronic, and phonon entropies, which are all stabilizing for defects, therefore have uncommonly large stabilizing effects.

IV. CONCLUSIONS

In simulations of a ZrC crystal, five distinct carbon Frenkel defect configurations have been found that are metastable at zero temperature. Two of the configurations are bound pairs and in three other configurations the vacancy and interstitial are separated. While at 300 K the equilibrium concentration of Frenkel pairs is negligible, at 3200 K they were frequent enough to occur spontaneously during a first-principles molecular dynamics simulation.

We have performed quasiharmonic lattice dynamics calculations to study further the thermodynamics of these defects. The results indicate surprisingly high concentrations of bound and unbound Frenkel pairs: in the stoichiometric crystal we estimate 0.01% per mole at 2000 K, 0.2% at 2500 K, and 1.2% at 3000 K. For a substoichiometric crystal we can predict how much the number would be suppressed by recombination. The

high proportion of bound vacancy-interstitial pairs maintains the high concentration of Frenkel pairs even in the presence of constitutional vacancies. We find for $ZrC_{0.9}$ at 3000 K the concentration is reduced from the stoichiometric value 1.2% to 0.3%. This is by reducing the concentration of bound pairs from 0.93% to 0.07%, and the unbound pairs from 0.27% to 0.24%.

The high concentration of Frenkel defects changes the properties of ZrC several important ways. A concentration of one defect per 64 atom ZrC cell approximately doubles the electronic density of states at the Fermi level, decreases the bulk modulus by 8–18 GPa, and dilates the lattice by 0.1%–0.15%. The Frenkel contribution to the heat capacity is relatively small for moderate temperatures, not exceeding 0.05 k_B for $T < 2000$ K, but the rate of increase suggests it will be much larger near the melting point.

ACKNOWLEDGMENTS

T.A.M. and M.W.F. acknowledge the financial support of EPSRC Programme Grant Material Systems for Extreme Environments (XMat) (Grant No. EP/K008749/2), EPSRC Programme Grant Carbides for Future Fission Environments (CAFFE) (Grant No. EP/M018563/1), and H2020 Project Grant Il Trovatore (Grant No. 740415). T.A.M. and M.W.F. acknowledge computational resources from the UK Materials and Molecular Modelling Hub (Grant No. EP/P020194/1) and embedded CSE 33 of the ARCHER UK National Supercomputing Service (http://www.archer.ac.uk). A.I.D. would like to thank the STFC Hartree Centre for supporting this effort by allowing human resource to be dedicated to this work. This work was in part supported by the STFC Hartree Centre's Innovation: Return on Research programme, funded by the UK Department for Business, Energy & Industrial Strategy.

APPENDIX A: IDEAL SOLUTION MODEL

We derive an ideal solution model for ZrC based on the configurational entropy of the carbon sublattice. The articles of interest on the lattice are constitutional carbon vacancies (denoted N_1), bound Frenkel pairs (N_2), and unbound Frenkel pairs (N_3). The basis for counting combinations of these species is the number of perfect sites ($N - N_1 - N_2 - 2N_3$), the number of vacancies ($N_1 + N_3$), bound pairs (N_2) and free interstitials (N_3). The number of combinations or unordered selections without repetition is

$$Z = m_2^{N_2} m_3^{N_3} \frac{N!}{(N - N_1 - N_2 - 2N_3)!\,(N_1 + N_3)!\,N_2!\,N_3!}.$$

Factors m_2 and m_3 account for the degeneracy of interstitial sites for bound pairs and unbound pairs, with m_2 counted with respect to carbon vacancy sites and m_3 with respect to carbon perfect lattice sites.

The first-order Stirling approximation is applied to the lattice configurational entropy

$$S^{\mathrm{mix}} = \ln Z\,,$$

giving the expression

$$\begin{aligned} S^{\mathrm{mix}} = {} & N_2 \ln m_2 + N_3 \ln m_3 + N \ln N \\ & - (N - N_1 - N_2 - 2N_3) \ln (N - N_1 - N_2 - 2N_3) \\ & - (N_1 + N_3) \ln (N_1 + N_3) - N_2 \ln N_2 - N_3 \ln N_3. \end{aligned}$$

The Gibbs free energy of the system of defects

$$\sum_{i=1}^{i=3} N_i \Delta G_i = T S^{\mathrm{mix}}\,,$$

is minimised with respect to the number of each type of defect

$$\Delta G_i = T \partial_{N_i} S^{\mathrm{mix}}.$$

For bound pairs the configuration entropy term is

$$\partial_{N_2} S^{\mathrm{mix}} = \ln \frac{m_2\,(N - N_1 - N_2 - 2N_3)}{N_2}\,,$$

and for unbound pairs

$$\partial_{N_3} S^{\mathrm{mix}} = \ln \frac{m_3\,(N - N_1 - N_2 - 2N_3)^2}{(N_1 + N_3) N_3}.$$

The free energies to form bound and unbound pairs are given by

$$\Delta G_2 = T \ln \frac{m_2 (N - N_1 - N_2 - 2N_3)}{N_2}\,,$$

and

$$\Delta G_3 = T \ln \frac{m_3 (N - N_1 - N_2 - 2N_3)^2}{(N_1 + N_3) N_3}.$$

The concentrations ($n_i = N_i / N$) of each defect type are

$$n_2 = (1 - n_1 - n_2 - 2n_3) m_2 \exp\left(-\frac{\Delta G_2}{T}\right),$$

and

$$n_3 = \frac{(1 - n_1 - n_2 - 2n_3)^2}{(n_1 + n_3)} m_3 \exp\left(-\frac{\Delta G_3}{T}\right).$$

For completeness the concentration of each subtype of defect is stated explicitly. For bound pairs, the concentrations of dimer and trimer configurations are

$$n_{B_2} = \left[1 - n_1 - n_{B_2} - n_{B_3} - 2\left(n_{U_2} + n_{U_3} + n_{U_4}\right)\right] m_{B_2} \exp\left(-\frac{\Delta G_{B_2}}{T}\right),$$

$$n_{B_3} = \left[1 - n_1 - n_{B_2} - n_{B_3} - 2\left(n_{U_2} + n_{U_3} + n_{U_4}\right)\right] m_{B_3} \exp\left(-\frac{\Delta G_{B_3}}{T}\right),$$

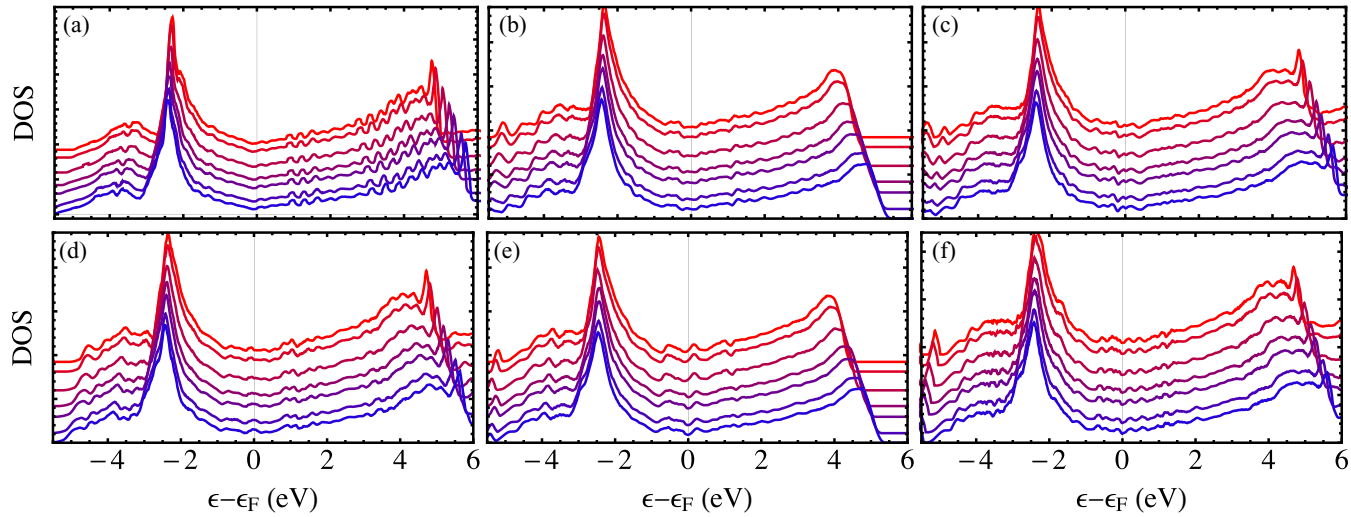

FIG. 10. Electron density of states as a function of dilation. (a) Perfect ZrC, (b) B_2 bound dimer, (c) B_3 bound trimer, (d) U_2 unbound dimer, (e) U_3 unbound trimer, (f) U_4 unbound tetramer. Thermal expansion increases from blue to red. Consecutive densities of states are shifted up proportional to the increase in volume.

and the concentrations of unbound Frenkel pairs of dimer, trimer and tetramer configurations are

$$n_{U_2} = \frac{\left[1 - n_1 - n_{B_2} - n_{B_3} - 2\left(n_{U_2} + n_{U_3} + n_{U_4}\right)\right]^2}{\left(n_1 + n_{U_2} + n_{U_3} + n_{U_4}\right)} m_{U_2} \exp\left(-\frac{\Delta G_{U_2}}{T}\right),$$

$$n_{U_3} = \frac{\left[1 - n_1 - n_{B_2} - n_{B_3} - 2\left(n_{U_2} + n_{U_3} + n_{U_4}\right)\right]^2}{\left(n_1 + n_{U_2} + n_{U_3} + n_{U_4}\right)} m_{U_3} \exp\left(-\frac{\Delta G_{U_3}}{T}\right),$$

$$n_{U_4} = \frac{\left[1 - n_1 - n_{B_2} - n_{B_3} - 2\left(n_{U_2} + n_{U_3} + n_{U_4}\right)\right]^2}{\left(n_1 + n_{U_2} + n_{U_3} + n_{U_4}\right)} m_{U_4} \exp\left(-\frac{\Delta G_{U_4}}{T}\right).$$

APPENDIX B: ELECTRON STATES

Figure 4 in the main text shows the electron density of states for each defect on the interval $[-0.5, 0.5]$ eV. The density of states is provided for interval $[-6, 6]$ eV in Fig. 10.

[1] S. Kim, I. Szlufarska, and D. Morgan, *Ab initio* study of point defect structures and energetics in ZrC, J. Appl. Phys. **107**, 053521 (2010).

[2] V. I. Razumovskiy, A. V. Ruban, J. Odqvist, and P. A. Korzhavyi, Vacancy-cluster mechanism of metal-atom diffusion in substoichiometric carbides, Phys. Rev. B **87**, 054203 (2013).

[3] R. W. Harrison and W. E. Lee, Processing and properties of ZrC, ZrN and ZrCN ceramics: A review, Adv. Appl. Cer. **115**, 294 (2016).

[4] J. F. Justin and A. Jankowiak, Ultra high temperature ceramics: Densification, properties and thermal stability, AerospaceLab **3**, 1 (2011).

[5] A. I. Duff, T. Davey, D. Korbmacher, A. Glensk, B. Grabowski, J. Neugebauer, and M. W. Finnis, Improved method of calculating ab initio high-temperature thermodynamic properties with application to ZrC, Phys. Rev. B **91**, 214311 (2015).

[6] A. I. Savvatimskiy, S. V. Onufriev, and S. A. Muboyadzhyan, Measurement of ZrC properties up to 5000 K by fast electrical pulse heating method, J. Mater. Res. **32**, 1557 (2017).

[7] A. Fernández Guillermet, Analysis of thermochemical properties and phase stability in the zirconium-carbon system, J. Alloys Compd. **217**, 69 (1995).

[8] T. Davey, Thermodynamic assessments of the (Zr,Hf) carbides and borides revisited and informed by the calculation of defect formation energies in ZrC, Ph.D. thesis, Imperial College London, 2017.

[9] Y. Zhang, J. Wang, J. Wang, B. Liu, and H. Zhang, Understanding the behavior of native point defects in ZrC by first-principles calculations, J. Amer. Cer. Soc. **97**, 4024 (2014).

[10] G. Kresse and J. Furthmüller, Efficiency of ab-initio total energy calculations for metals and semiconductors using a plane-wave basis set, Comput. Mater. Sci. **6**, 15 (1996).

[11] G. Kresse and J. Furthmüller, Efficient iterative schemes for ab initio total energy calculations using a planewave basis set, Phys. Rev. B **54**, 11169 (1996).

[12] J. P. Perdew and A. Zunger, Self-interaction correction to density-functional approximations for many-electron systems, Phys. Rev. B **23**, 5048 (1981).

[13] G. Kresse and D. Joubert, From ultrasoft pseudopotentials to the projector augmented-wave method, Phys. Rev. B **59**, 1758 (1999).
[14] A. Togo and I. Tanaka, First principles phonon calculations in materials science, Scr. Mater. **108**, 1 (2015).
[15] G. Kresse, J. Furthmüller, and J. Hafner, *Ab initio* force constant approach to phonon dispersion relations of diamond and graphite, Europhys. Lett. **32**, 729 (1995).
[16] K. Parlinski, Z. Li, and Y. Kawazoe, First-Principles Determination of the Soft Mode in Cubic ZrO_2, Phys. Rev. Lett. **78**, 4063 (1997).
[17] A. Togo, F. Oba, and I. Tanaka, First-principles calculations of the ferroelastic transition between rutile-type and $CaCl_2$-type SiO_2 at high pressures, Phys. Rev. B **78**, 134106 (2008).
[18] M. Methfessel and A. T. Paxton, High-precision sampling for Brillouin-zone integration in metals, Phys. Rev. B **40**, 3616 (1989).
[19] N. D. Mermin, Thermal properties of the inhomogeneous electron gas, Phys. Rev. **137**, A1441 (1965).
[20] K. Momma and F. Izumi, VESTA 3 for three-dimensional visualization of crystal, volumetric and morphology data, J. Appl. Crystallogr. **44**, 1272 (2011).
[21] M. J. Gillan and P. W. M. Jacobs, Entropy of a point defect in an ionic crystal, Phys. Rev. B **28**, 759 (1983).
[22] A. Walsh, A. A. Sokol, and C. R. A. Catlow, Free energy of defect formation: Thermodynamics of anion Frenkel pairs in indium oxide, Phys. Rev. B **83**, 224105 (2011).
[23] P. W. M. Jacobs, M. A. H. Nerenberg, J. Govindarajan, and T. M. Haridasan, The entropy of formation of anion Frenkel defects in fluorites: A quasiharmonic calculation for calcium fluoride, J. Phys. C **15**, 4245 (1982).
[24] V. C. Sahni and P. W. M. Jacobs, A calculation of the vibrational entropy of anion Frenkel defects in fluorite crystals, Philos. Mag. A **46**, 817 (1982).
[25] H. Ihara, M. Hirabayashi, and H. Nakagawa, Electronic band strutures and x-ray photoelectron spectra of ZrC, HfC and TaC, Phys. Rev. B **14**, 1707 (1976).
[26] A. S. Borukhovich and P. V. Geld, Magnetic susceptibility and energy band structure of zirconium monocarbide, Phys. Status Solidi **36**, 97 (1969).
[27] A. Arya and E. A. Carter, Structure, bonding, and adhesion at the ZrC(100)/Fe(110) interface from first principles, Surf. Sci. **560**, 103 (2004).
[28] D. G. Pettifor, Theory of energy bands and related properties of 4d transition metals. I. Band parameters and their volume dependence, J. Phys. F **7**, 613 (1977).
[29] M. Jiang, J. W. Zheng, H. Y. Xiao, Z. J. Liu, and X. T. Zu, A comparative study of the mechanical and thermal properties of defective ZrC, TiC and SiC, Sci. Rep. **7**, 9344 (2017).
[30] V. I. Ivashchenko, P. E. A. Turchi, and V. I. Shevchenko, First-principles study of elastic and stability properties of ZrC-ZrN and ZrC-TiC alloys, J. Phys.: Condens. Matter **21**, 395503 (2009).
[31] D. Cheng, S. Wang, and H. Ye, First-principles calculations of the elastic properties of ZrC and ZrN, J. Alloys Compd. **377**, 221 (2004).
[32] P. T. Jochym and K. Parlinski, Ab initio lattice dynamics and elastic constants of ZrC, Eur. Phys. J. B **15**, 265 (2000).
[33] C. Xie, A. R. Oganov, D. Li, T. T. Debela, N. Liu, D. Dong, and Q. Zeng, Effects of carbon vacancies on the structures, mechanical properties, and chemical bonding of zirconium carbides: A first-principles study, Phys. Chem. Chem. Phys. **18**, 12299 (2016).
[34] R. Chang and L. J. Graham, Low-temperature elastic properties of ZrC and TiC, J. Appl. Phys. **37**, 3778 (1966).
[35] C. R. F. Azevedo, Selection of fuel cladding material for nuclear fission reactors, Eng. Fail. Anal. **18**, 1943 (2011).
[36] C. Jiang, M. J. Zheng, D. Morgan, and I. Szlufarska, Amorphization Driven by Defect-Induced Mechanical Instability, Phys. Rev. Lett. **111**, 155501 (2013).
[37] Y. Katoh, L. L. Snead, I. Szlufarska, and W. J. Weber, Radiation effects in SiC for nuclear structural applications, Curr. Opin. Solid State Mater. Sci. **16**, 143 (2012).
[38] L. S. Snead, T. Nozawa, Y. Katoh, T.-S. Byun, S. Kondo, and D. A. Petti, Handbook of SiC properties for fuel performance modeling, J. Nucl. Mater. **371**, 329 (2007).
[39] A. C. Marino, E. L. Losada, G. L. Demarco, and L. Furlano, A safety fuel element assessment by using new materials and advanced modelling tools, Technical report, 2015.
[40] K. J. Geelhood, W. G. Luscher, C. E. Beyer, and M. E. Flanagan, FRAPCON-3.4: A Computer Code for the Calculation of Steady State Thermal-mechanical Behavior of Oxide Fuel Rods for High Burnup, Richland, WA: US Nuclear Regulatory Commission, Office of Nuclear Regulatory Research (2011).
[41] R. Liu, W. Zhou, and J. Cai, Multiphysics modeling of accident tolerant fuel-cladding U_3Si_2-FeCrAl performance in a light water reactor, Nucl. Eng. Des. **330**, 106 (2018).
[42] R. Devanathan, L. Van Brutzel, A. Chartier, C. Guéneau, A. E. Mattsson, V. Tikare, T. Bartel, T. Besmann, M. Stan, and P. Van Uffelen, Modeling and simulation of nuclear fuel materials, Ener. Env. Sci. **3**, 1365 (2010).
[43] E. V. Safonova, Y. P. Mitrofanov, R. A. Konchakov, A. Yu Vinogradov, N. P. Kobelev, and V. A. Khonik, Experimental evidence for thermal generation of interstitials in a metallic crystal near the melting temperature, J. Phys.: Condens. Matter **28**, 215401 (2016).